# Electrode plasma formation and melt in *Z*-pinch accelerators

N. Bennett,[1] D. R. Welch,[2] K. Cochrane,[1] K. Leung,[1] C. Thoma,[2]
M. E. Cuneo,[1] and G. Frye-Mason[1]

[1]*Sandia National Laboratories, Albuquerque, New Mexico 87185, USA*
[2]*Voss Scientific, LLC, Albuquerque, New Mexico 87108, USA*

(Received 1 February 2023; accepted 4 April 2023; published 25 April 2023)

Recent studies of power flow and particle transport in multi-MA pulsed-power accelerators demonstrate that electrode plasmas may reduce accelerator efficiency by shunting current upstream from the load [Bennett *et al.*, Phys. Rev. Accel. Beams **24**, 060401 (2021)]. The detailed generation and evolution of these electrode plasmas are examined here using fully relativistic, Monte Carlo particle-in-cell (PIC) and magnetohydrodynamic (MHD) simulations over a range of peak currents (8–48 MA). The PIC calculations, informed by vacuum science, describe the electrode surface breakdown and particle transport prior to electrode melt. The MHD calculations show the bulk electrode evolution during melt. The physical description provided by this combined study begins with the rising local magnetic field that increases the local electrode surface temperature. This initiates the thermal desorption of contaminants from the electrode surface, with contributions from atoms outgassing from the bulk metal. The contaminants rapidly ionize forming a $10^{15}$–$10^{18}$ cm$^{-3}$ plasma that is effectively resistive while weakly collisional because it is created within, and rapidly penetrated by, a strong magnetic field (> 30 T). Prior to melting, the density of this surface plasma is limited by the concentration of absorbed contaminants in the bulk ($\sim 10^{19}$ cm$^{-3}$ for hydrogen), its diffusion, and ionization. Eventually, the melting electrodes form a conducting plasma ($10^{21}$–$10^{23}$ cm$^{-3}$) that experiences $\mathbf{j} \times \mathbf{B}$ compression and a typical decaying magnetic diffusion profile. This physical sequence ignores the transport of collisional plasmas of $10^{19}$ cm$^{-3}$ which may arise from electrode defects and associated instabilities. Nonetheless, this picture of plasma formation and melt may be extrapolated to higher-energy pulsed-power systems.

DOI: 10.1103/PhysRevAccelBeams.26.040401

## I. INTRODUCTION

The pulsed-power accelerators that drive *Z*-pinch and dynamic material properties (DMPs) experiments achieve some of the highest current densities (> 1 MA/cm$^2$) in routine laboratory operation. These densities are typically arrived at through radially converging transmission lines. Currents are added at larger radii and transported radially inward to achieve the desired current density for driving the *Z*-pinch [1–7]. The vacuum transmission lines are low inductance, with small anode-cathode (AK) gaps, to efficiently couple to the pinch. The resulting electric field stresses on the cathodes typically exceed thresholds for electron emission [8,9], and this free current is rapidly magnetically insulated. The vacuum sections, thus, transition to magnetically insulated transmission lines (MITLs) during the pulse. As the current density increases nearer the load, Joule heating and particle energy deposition lead to the formation of surface plasmas. This process begins with the emission of sorbed electrode contaminants and may progress through melt.

While rapid heating through melt is desired for an imploding-liner load, the electrode plasmas formed upstream in the transmission line may reduce an accelerator's efficiency. This occurs when plasma is transported into the AK gap enabling a cross-gap current, referred to as "current loss" [10,11]. Susceptible systems include the Z accelerator at Sandia National Laboratories [1,12,13], the Primary Test Stand (PTS) at the China Academy of Engineering Physics [5,14], the Angara-5-1 Facility [2], and the GIT-12 and MIG generators at the Institute of High Current Electronics [15,16]. Recent studies focused on the Z Accelerator have determined that low-density AK-gap plasmas (< $10^{17}$ cm$^{-3}$ [17]) account for this current loss [18].

The electrode operating conditions in pulsed-power *Z*-pinch drivers range from near vacuum to charged particle emission, then to surface/bulk contaminant desorption, and ultimately melt. A transmission-line segment will transition through some or all of these conditions over the course of a pulse. Further, these conditions exist simultaneously at different radii or local current density. The vacuum to

charged particle emission stages describe MITL conditions that are well understood [19–22] and previously modeled [23–25]. The desorption of surface contaminants has long been accepted [26–29] but more recently modeled for multi-MA systems [30–32]. These recent models capture the physics of vacuum through contaminant desorption but simplify the electrode plasma formation and neglect melt. These approximations are addressed in this paper using fully relativistic particle-in-cell (PIC) simulations of desorption and ionization (surface breakdown) and magnetohydrodynamic (MHD) models of melting electrodes. These simulations are conducted using dimensions and pulses relevant to Sandia's Z accelerator.

This combined modeling effort, with electrode outgassing, informed by vacuum sciences [26,28] and density functional theory (DFT) [33], presents a picture in which there are two surface plasma regimes in a multi-MA accelerator. The first one to form is comprised of light ions [28] at lower density ($10^{15}$–$10^{18}$ cm$^{-3}$). This is the electrode surface plasma formed from sorbed contaminants within the full strength of the magnetic field. (The neutrals desorb, expand, and ionize within the rising magnetic field.) The magnetic diffusivity remains high; it conducts a negligible amount of the total current. It may be nonneutral and has steep density and temperature gradients directed into the AK gap, where it may be considered collisionless. The $q\mathbf{E}$ term in the Lorentz equation contributes significantly to particle motion. As the electrode temperatures exceed melt locally, the surface metal layers form a second, near-solid-density plasma. These conducting plasmas are subject to $\mathbf{j} \times \mathbf{B}$, with diffusion into the AK gap of $\lesssim$100 μm and are well described by MHD.

This reduction to two principle plasma environments is based on the expectation of a limited supply of sorbed contaminants, limiting the peak plasma density prior to melt. This picture does not capture collisional plasmas of $10^{19}$–$10^{21}$ cm$^{-3}$ that lie in the midrange of magnetic diffusivity. These plasmas sources include wire array ablation [34] and asymmetric implosions, such as result from the electrothermal instability [35]. Experiments on the Z accelerator dedicated to measuring plasma densities in the AK gap have not observed densities in the $10^{19}$ cm$^{-3}$ regime [36].

In addition, this model-generated picture is subject to experimental validation, although the measured densities of $10^{16}$–$10^{17}$ cm$^{-3}$ [11,17] agree to date, 22.5-MA load currents have been reproduced with our model [31], and more publications for 18- to 20-MA current comparisons are in progress [37,38]. The simulations of electrode plasma formation presented in Sec. III assume a contaminant inventory and do not adjust the desorption rate, or process, during the phase transition. However, one conclusion from the breakdown simulations is the transport of plasma into the AK gap is sensitive primarily to the conditions at its vacuum interface and not on the electrode surface.

The imposed limits on the surface plasma as mainly hydrogen, absorbed into and adsorbed on the electrode metal lattice, are supported in Sec. II. The first-principles simulations of electrode plasma formation and transport are described in Sec. III, with implications for plasma transport discussed in Sec. IV. Melting electrodes in a *Z*-pinch accelerator are described in Sec. V.

## II. ELECTRODE COMPOSITION CONTRIBUTING TO PLASMA FORMATION

It has long been noted that outgassing from heated metals is dominated by $H_2O$ and $H_2$ [27,28]. In thermal outgassing measurements, $H_2O$ is the main component initially [39,40], accounting for 80%–90% of the partial pressure for stainless steel [41]. Anode plasma formation temperatures appear consistent with binding energies associated with $H_2O$ [29]. Over longer periods and higher temperatures, $H_2$ desorption persists [39,42], accounting for over 95% of the residual gas [40]. The other constituents observed are CO, $CO_2$, $CH_4$, and other hydrocarbons, with no observable contribution from metal constituents (Fe, Cr, Ni, Mn, or Au) prior to vaporization [10,27,29].

The rate of desorption is calculated from the Arrhenius equation and an adsorption isotherm describes the surface coverage of the contaminant gas. Of these, the Temkin isotherm can successfully explain the surface-density dependence of $E'(n)$ seen in molecular dynamics simulations [43] and the time-dependence of outgassing measurements [26].

When the theoretical and experimental outgassing rates are integrated, however, the amount of gas exceeds the maximum surface density by as much as 100 times [26]. For an atomically smooth transition metal, the surface density is of order $10^{15}$ particles/cm$^2$ and is referred to as a monolayer (ML). The amount of gas measured in thermal outgassing experiments ranges from 3 to 100 ML [27,44]. This surplus may be accounted for by hydrogen entrained in steel during fabrication. The absorbed hydrogen may reach weight concentrations of a few parts per million [40,45] or $10^{19}$ cm$^{-3}$. The inventory available for plasma formation is thus limited by the penetration depth of the (time-dependent) magnetic field in the metal, as discussed in Sec. V, and by the diffusion of hydrogen through the metal lattice. (Measured diffusion rates range from $3.5 \times 10^{-8}$ cm$^2$/s at 300 °C to $8.7 \times 10^{-5}$ cm$^2$/s at 1000 °C [39,46].) For a melt depth of 10–100 μm, the equivalent of ∼10–100 ML could be released, but the hydrogen diffusion rate for electrodes heated to melt on ns timescales is unknown.

This process of $H_2$ desorption has long been described as taking place "in two zones: atomic hydrogen migration through the bulk material, atomic hydrogen recombination at the surface, and molecular hydrogen desorption from the surface" [40]. A number of desorption analyses take as the

starting point that the rate is limited by diffusion from the bulk metal and near-surface layers [27,46,47]. For steel, $H_2O$ may be desorbed via oxide reduction chemistry by hydrogen reactions with the surface oxide layer through the following two reactions [44,48]

$$Fe_xO_y + 2H \rightarrow Fe + H_2O$$
$$Cr_2O_3 + 6H \rightarrow 2Cr + 3H_2O.$$

The energetics and rates of these reactions and hydrogen diffusion are being studied using DFT [49].

Based on these results from vacuum science, $H_2$ is used as the electrode contaminant species in the surface breakdown models described in Sec. III A. The other contaminant masses are not considered. The assumed $H_2$ inventory is within the typical measured range; however, the rate of hydrogen diffusion through bulk metal is unknown for electrodes undergoing melt. The existing outgassing experiments [27,40,44,46] use temperature ramp rates measured in seconds to hours which lead to significant hydrogen reduction before high temperatures are reached. We are pursuing modeling and measurement techniques to determine the diffusion rate in pulse power systems. At present, it is the largest uncertainty in the model discussed in Sec. III A.

## III. ELECTRODE PLASMA FORMATION

The electrode surface plasma formation is modeled from first principles in order to identify the breakdown timescales, the ionization fractions, and the impact of neutrals on transport. The model is constructed using a segment of a coaxial transmission line operating at the multi-MA-scale, relevant to the Z Accelerator. This configuration is illustrated in Fig. 1, which shows an example of a coaxial line fielded on Z [Fig. 1(a)] and the test configuration it motivated [Fig. 1(b)].

The surface breakdown is modeled kinetically using a Monte Carlo PIC treatment [50–52] in the fully relativistic electromagnetic PIC code CHICAGO [32,53–56]. The simulations track the injection of a voltage pulse, electrode heating, charged particle emission, desorption of neutral contaminants, and subsequent particle interactions. The interactions determined to be significant are ionization, momentum exchange, and charge exchange, as detailed in Sec. III A.

Not included in the model is an influx of non-neutral plasma generated along the upstream electrodes and a load region that terminates the plasma flow. The accumulation of plasma in the inner MITL, visible in Fig. 1(a), increases the density that spans the AK gap and contributes to current loss [18]. While important in power-flow models, it is neglected here to reduce the required compute resources. Those surface contaminants with low mobility are neglected for the same reason. The simulations thus track only desorbed $H_2$ and its constituents (excluding excited states), but still exceed 1.5 billion particles in 3.75 million cells.

The surface breakdown is modeled for three rates of current rise with results discussed in Sec. III B. For comparison, a fourth simulation assumes the desorbed $H_2$ is fully ionized within three grid cells from the surface. This assumption is made in studies of current delivery on the Z Accelerator and its verification is performed here, with $H_2$ replacing the $H_2O$ plasma modeled in Refs. [30,31], and [18].

### A. Kinetic breakdown model

The 2D cylindrical $(r, z)$ geometry used in the kinetic breakdown models is illustrated in Fig. 1(b). A voltage pulse with a linear rise is injected from the left at $z = 0$. The impedance of the outlet boundary at the right ($z = 3$ cm) is selected to achieve current rises of 80 kA/ns, 280 kA/ns, and 480 kA/ns. These pulses roughly correspond to DMP experiments on the Z accelerator, fast $Z$-pinch experiments on Z, and an upgraded system with 48-MA peak current. The simulations are run only through breakdown and, as a result, the particle emission does not reach equilibrium, as shown in the density contours in Fig. 1(b). The surface temperatures and electric field stresses are higher closer to the injection port.

The simulations use a magnetic-implicit solver to advance the fields and particles [57], although the cyclotron

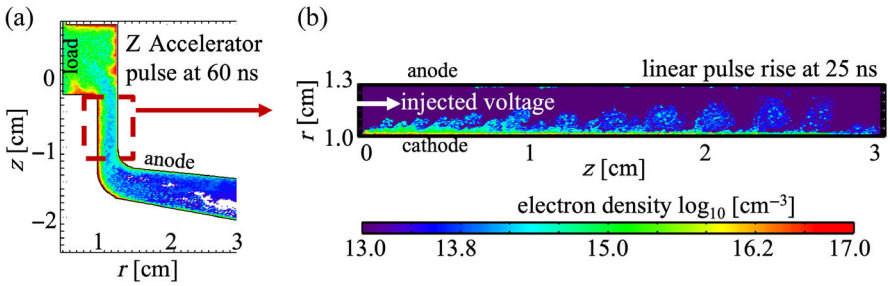


FIG. 1. (a) An example of the inner transmission line on the Z Accelerator (from Ref. [18]) in which electrode plasma formation and plasma influx shunts current across the gap. (b) The simulation geometry for first-principles electrode plasma formation (without plasma influx). The electron density contours are shown for both on the same $\log_{10}$ scale ($10^{13}$–$10^{17}$), but the simulation times are not comparable.

motion is resolved with $\omega_c \Delta t \leq 0.5$. A cloud-in-cell model is used to minimize electrostatic fluctuations from individual macroparticles [58], and a time-biasing algorithm [59] is used to control the growth of electromagnetic fluctuations on the grid. A grid spacing of $\Delta r, z = 4$ μm resolves the fields in the sheath that impact, and are impacted by, evolving space charges. The resolution is relaxed to 10 μm for the simulation that assumes the desorbed $H_2$ is fully ionized within three grid cells.

The electrode surfaces are continuously updated for local temperature increases from Joule heating and particle energy deposition. The Joule heating model derives from [60]

$$T_J(t) = \frac{1}{c_v}\int_0^t \frac{j^2(t)}{\sigma}dt,$$

where $\sigma$ and $c_v$ are the conductivity and specific heat of the electrode material (assumed constant), and $j$ is the lineal current density: $j(t) = \partial H(x,t)/\partial x$, where $H = B/\mu_0$ and $x$ is the coordinate normal to the conducting surface cell. Assuming a linearly rising $j(t)$ and that magnetic field diffusion is the dominant contributor over heat conduction, the local temperature increase is

$$\Delta T_J(t) \approx \frac{\vartheta \mu_0 H^2(t)}{2c_v}, \tag{1}$$

which is Eq. 5.2–30 from Ref. [60] The surface energy factor $\vartheta = 1.273$ (from Table 5.2-II of Ref. [60] and $c_v = 3.9$ J/cm$^3$ K for stainless steel [61,62]. As noted in Ref. [60], the assumption of constant $\sigma$ underestimates the temperature rise but is valid for small $\delta T/T$. (The conductivity of stainless decreases from 1.3 MΩm at 300 K to 0.9 MΩm at 1100 K [63]).

Particle energy deposition ($dE/ds$) is calculated using the Bethe-Bloch equations for electron and ion energy loss [64]. The path length in a grid cell is $ds = dx/\cos\theta$, where $dx$ is the cell depth and $\theta$ is the particle angle of incidence. The temperature increase $[T_d(t)]$ per macroparticle is then calculated as

$$\Delta T_d = \frac{dE}{ds}\frac{q}{ec_v A}, \tag{2}$$

where $q$ is the macroparticle charge, $e$ is the electron charge, and $A$ is the cell's surface area.

Charged-particle emission is modeled as both field-induced and thermal emission from the electrode surfaces. Electrons are emitted from the cathode after the local electric field stress exceeds the tolerance of the conductor [8], where 240 kV/cm [65] is used here for stainless steel. Protons are emitted from the anode after the local surface temperature increases by 400 °C [29,66]. This proton emission is typical in power-flow models [23,25], but becomes negligible when plasma formation is also modeled. (The plasma density exceeds the thermal proton density by $\sim 10^4$.) The emission rate for these processes is space charge limited (SCL) [8], and dense surface plasmas alter the electric fields adjacent to the electrodes.

Charged particle collisions use a binary Coulomb collision model derived from Ref. [67], in which Nanbu's theory of the cumulative property of Coulomb collisions is applied by sampling the velocities of surrounding particles. The Coulomb collision frequency is given by Spitzer for species $\alpha$ scattering off species $\beta$ [68]:

$$\nu_{\alpha\beta} = \frac{4\sqrt{2\pi}e^4 Z_\alpha^2 Z_\beta^2 n_\beta \ln\Lambda_{\alpha\beta}}{(4\pi\epsilon_0)^2\, 3m_\alpha\mu_{\alpha\beta}}\left(\frac{T_\alpha}{m_\alpha}+\frac{T_\beta}{m_\beta}\right)^{-3/2}, \tag{3}$$

where $\mu_{\alpha\beta} = m_\alpha m_\beta/(m_\alpha + m_\beta)$ and $\ln\Lambda_{\alpha\beta}$ is the Coulomb logarithm.

Neutral ($H_2$) surface contaminants are thermally desorbed from both electrodes using individual surface-cell temperatures. The Arrhenius equation calculates the thermal desorption rate as a function of the surface density of adsorbed contaminant particles $[n(t)]$:

$$\frac{dn(t)}{dt} = -\nu_{th} n(t)\, e^{-E'(n)/[k_B T(t)]}, \tag{4}$$

where $\nu_{th} \sim 10^{13}$ s$^{-1}$, $E'(n)$ is the effective binding energy, and $T$ is the local surface temperature [69,70]. The initial surface coverage is $n(0) = 2n_{ML}$, where $n_{ML} = 8\times 10^{15}$ particles/cm$^2$ is the hard-coded definition presently in CHICAGO [used in Eq. (5)]. This total 16 ML inventory is in the range for outgassing and consistent with models of current loss. The Temkin isotherm computes $E'(n)$ via

$$E'(n) = E_d\left(1-\alpha\frac{n(t)}{n_{ML}}\right) \quad [\text{eV}], \tag{5}$$

where $E_d$ is the binding energy at infinitesimal coverage and $\alpha$ is determined experimentally. For the values used, $E_d = 0.8$ eV is consistent with molecular dynamics calculations and $\alpha = 0.17$ is retained from comparisons of simulated currents to data [31], where measured and simulated 22.5-MA load currents agree within measurement uncertainty and to a physics-based transmission-line-circuit model of Z [71], which reproduces upstream currents to within 2%.

Neutral ionization is mostly the result of electron and ion impact, with electron-neutral and ion-neutral elastic and inelastic scattering modeled in Monte Carlo fashion [51,53] using measured cross sections. These cross sections are tabulated as functions of the incident particle's energy. Momentum transfer and charge exchange are similarly modeled using the PIC-Monte Carlo technique [72–74]. The ionization cross sections for the following reactions are included in the simulations and plotted in Figs. 2 and 3 for

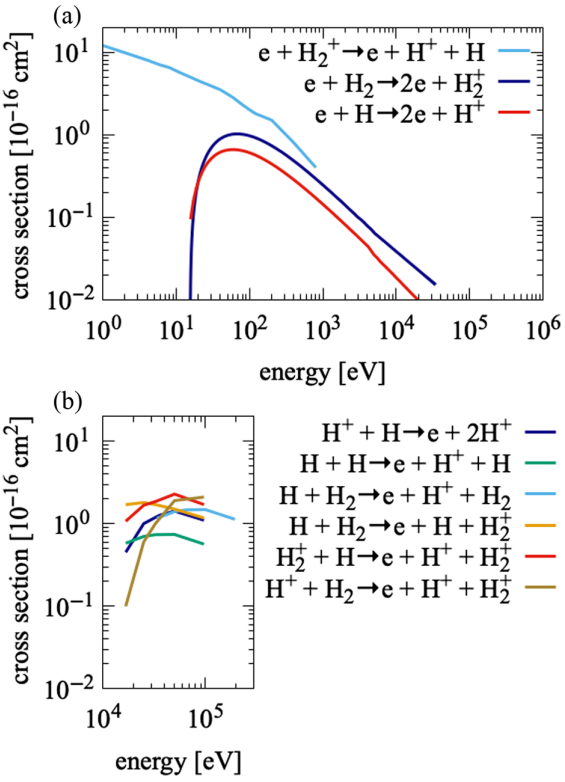


FIG. 2. The cross sections used in the breakdown model for (a) electron impact ionization and detachment [75,76,82] and (b) hydrogen impact ionization [78].

reference: $e + H \to 2e + H^+$ [75], $e + H_2 \to 2e + H_2^+$ [75], $e + H_2^+ \to e + H^+ + H$ [76], $H^+ + H \to e + 2H^+$ [77], $H + H \to e + H^+ + H$ [78], $H + H_2 \to e + H^+ + H_2$ [78], $H + H_2 \to e + H + H_2^+$ [78], $H^+ + H_2 \to e + H^+ + H_2^+$ [78], $H_2^+ + H \to e + H^+ + H_2^+$ [79], $H^+ + H \to H + H^+$ [80], $H^+ + H_2 \to H + H_2^+$ [80], $H_2^+ + H \to H^+ + H_2$ [80], $e + H_2^+ \to 2H$ [81].

Dissociative recombination is not plotted because its peak cross section of $10^{-20}$ cm$^2$ [81] is well below the ranges in Fig. 2. Attachment is not modeled because the cross sections for $e + H \to H^-$ and $e + H_2 \to H^- + H$ are negligible in the energy range of interest [83]. The processes for double ionization of $H_2$ are also not modeled because their cross sections are roughly 3 orders of magnitude smaller that those of single ionization [84]. Photoionization is neglected because cross sections are of order $10^{-18}$ cm$^2$ [85].

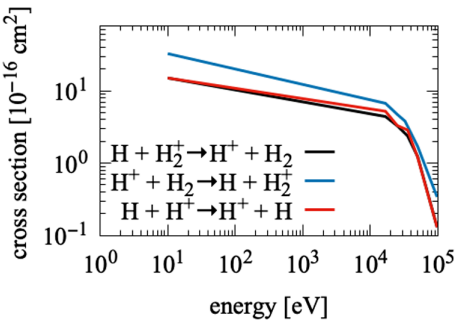


FIG. 3. Hydrogen charge exchange cross sections [80].

The energy dependencies of the rates in Figs. 2 and 3 indicate that, upon desorption of $H_2$, an $H_2^+$ population forms from impact with SCL-emitted electrons. The cross sections for $H_2^+$ fragmentation and charge exchange dominate, allowing the formation of neutral H via repetition of $e + H_2^+ \to e + H + H^+$ followed by $H^+ + H_2 \to H + H_2^+$. During this sequence, ions continue to be accelerated by the applied $\mathbf{E}$ and some of this energy is transferred to the neutrals. As the ions and neutrals accelerate, hydrogen impact ionization begins to contribute. The energy gain is limited, however, by magnetic insulation, as $\mathbf{v}_{\text{drift}} = \mathbf{E} \times \mathbf{B}/B^2$.

The relationship between $\mathbf{E}$ and $\mathbf{B}$ for a transmission line with a near short-circuit $Z$-pinch load is imperfectly captured in these simulations with a fixed outlet-boundary impedance. Nonetheless, the current rises are indicative of inductive loads with nonuniform $E/B$. The impacts of the magnetic field, both driving desorption and limiting ionization, are described in the next section.

### B. Surface breakdown

The magnetic field profiles generated from the three simulated pulses are plotted in Fig. 4(a). While the simulations are run only through breakdown, the electrode temperatures exceed melt in two cases (280 and 480 kA/ns). The desorption rates calculated from Eqs. (4) and (5), and assuming only Joule heating [Eq. (1)], are plotted in Fig. 4(b). The rates are normalized by $1/n$, but it is evident by the exponential dependence on temperature how rapidly an electrode surface is depleted in multi-MA operation.

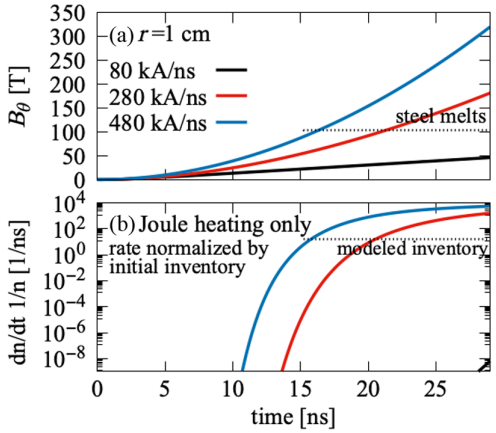


FIG. 4. (a) $B_\theta(t)$ at the cathode ($r = 1$ cm) in the kinetic breakdown simulations for the three current rises. The dashed line is the melting point from Eq. (1). (b) The normalized desorption rates from Eqs. (4) and (5) for the three current rises calculated from Joule heating [Eq. (1)] only. The dashed line represents the assumed inventory.

Joule heating dominates the electrode heating for the 280 and 480 kA/ns pulses, and the rates in Fig. 4(b) closely approximate those in the simulations. Without resupply, the contaminant inventories are depleted by 14 ns for the 480 kA/ns pulse and 17 ns at 280 kA/ns. At 80 kA/ns, however, Joule heating generates only the scant $10^{-8}$ ML/ns desorption rate appearing in Fig. 4(b) at 27 ns. Desorption actually occurs earlier and faster in this simulation, indicating that particle energy deposition effectively elevates surface temperatures as well.

While Fig. 4 highlights the differences driven by pulse rise, we first note the commonalities in the simulation results. The identical contaminant inventories used in the three pulses generate similar peak plasma densities seen in Fig. 5. The electron density distributions are surrogates for the multispecies plasmas, which have migrated from the cathodes into the gap, for each pulse, by 26 ns. The anodes, with lower $j$, are only beginning to emit. Of note is how transport appears inversely proportional to current. While desorption initiates earlier for faster current rises, the higher $B_\theta$ leads to more insulated surface plasmas. This is discussed in Sec. IV.

The plasma distributions in Fig. 5 are roughly comprised of two populations, the denser plasma on the surface and the plasma that has accelerated into the gap. The electron temperature contours in Fig. 6 help make that distinction. Ionization proceeds in a manner described in Sec. III A except that the applied **E** field is screened by the denser surface plasma. This plasma advects the cathode potential, as shown in radial line-outs of $E_r$ in Fig. 7a. (The collisionless skin depth at $10^{17}$ cm$^{-3}$ density is 16.8 μm and $\omega_{pe} \sim 10^{13}$/s.) Particles near the surface of this sheath experience more acceleration into the gap, forming a hotter, lower-density plasma for which the ionization cross sections are lower.

The growth of this screening effect with plasma density is suggested in Figs. 8(c) and 8(d), which show the average kinetic energies of electrons and $H^+$. The electron energies are high initially when electrons are sourced from electric field stress. After the onset of desorption, indicated in Fig. 8(a), $H^+$ is formed from $H_2$ ionization and fragmentation, as described in Sec. III A. The $H^+$ energies are initially high enough to ionize $H_2$ and H [cross sections in Fig. 2(b)]. As the surface plasma density increases, it screens the **E** field and reduces the average energies.

To discuss the differences driven by pulse rise, we refer back to Fig. 4(b). Desorption occurs earlier at 480 kA/ns,

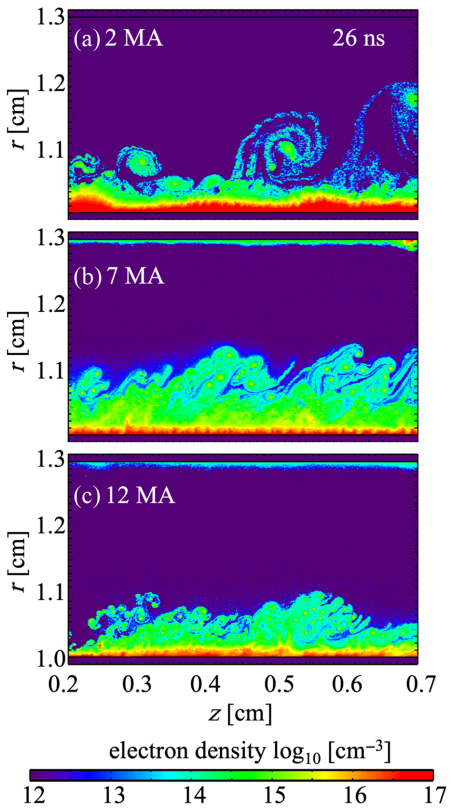


FIG. 5. The electron density contours in a 5-mm segment of the simulation illustrated in Fig. 1(b) at 26 ns reaching currents of (a) 2, (b) 7, and (c) 12 MA for the three pulse rises. Densities are plotted on a log scale from $10^{12}$–$10^{17}$.

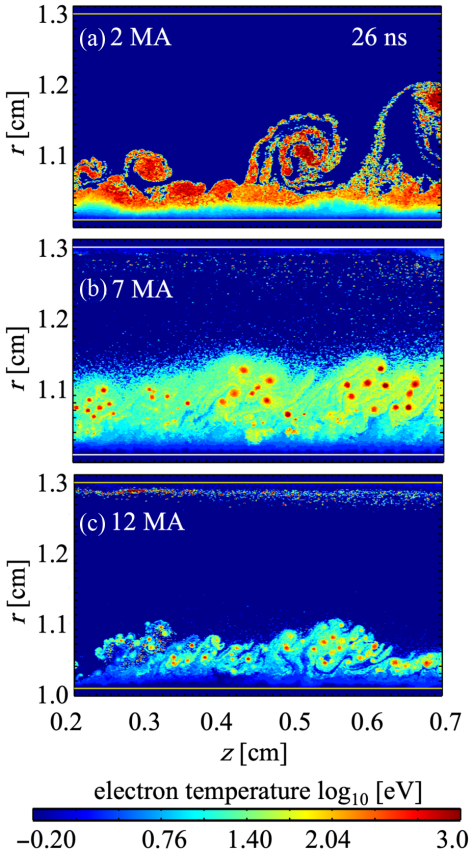


FIG. 6. The electron temperature contours corresponding to the densities in Fig. 5. The same 5-mm segment of the Fig. 1(b) simulation is used and the currents at 26 ns are (a) 2, (b) 7, and (c) 12 MA for the three pulse rises. Temperatures are plotted on a log scale from $10^{-2} - 10^{3}$.

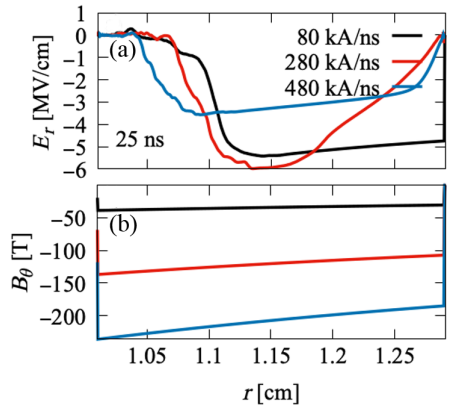


FIG. 7. (a) $E_r(r)$ averaged from $z = 0.3$–$1.0$ cm at 25 ns for the simulations in Fig. 5. Without particles, $E_r$ is constant across the gap and zero at the electrodes, similar to the 80 kA/ns trace at $r = 1.3$ cm which is before the anode plasma forms. The voltage drops are 990, 870, and 755 kV for 80, 280, and 480 kA/ns, respectively. (b) $B_\theta(r)$ at 25 ns. Note, the electrodes are perfect electric conductors in these kinetic simulations (Dirichlet boundary conditions).

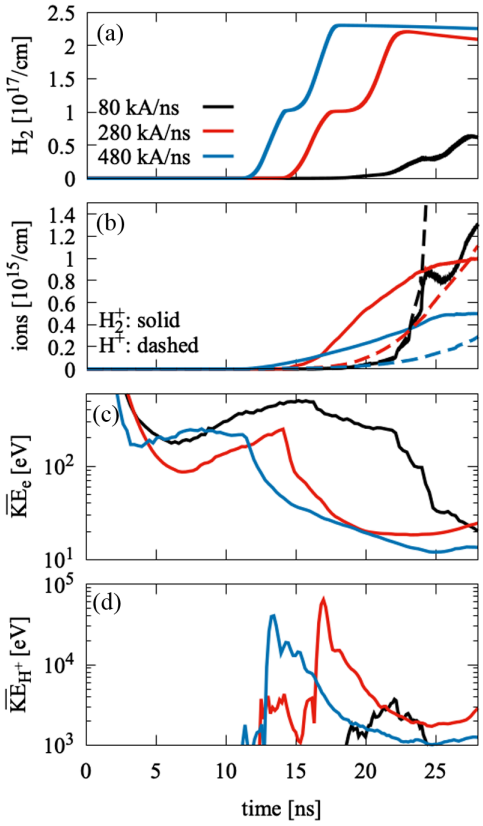


FIG. 8. (a) The average number of neutral $H_2$ per cm length of transmission line. (b) The average number of $H_2^+$ and $H^+$ ions per cm. The $H^+$ for 80 kA/ns exceed the scale, reaching $1.3 \times 10^{16}$/cm by 28 ns. (c) The average electron kinetic energy of the electrons. (d) The average $H^+$ kinetic energy of the protons.

followed a few ns later by the 280 kA/ns pulse. This is reflected in the $H_2$ levels in Fig. 8(a). For 80 kA/ns, the $H_2$ density rises later but ahead of the expectation from Joule-only heating in Fig. 4(b). The entire neutral inventory is liberated for the faster pulse rises, indicated by the approximate plateaus in Fig. 8(a).

Ionization is slower than desorption, comparing Figs. 8(a) and 8(b). Counterintuitively and inversely to the desorption rate, ionization slows as the energy density increases. This process is dictated by the interaction energies and Figs. 8(c) and 8(d) show the mean kinetic energies falling with increasing pulse rise. This trend is similar to $v_{\text{drift}}$, which also decreases with an increasing pulse because **B** rises faster than **E** (Fig. 7).

The dominant ionization processes early in the pulse are via electron impact. Referencing Fig. 8(d), the mean $H^+$ energies exceed the ionization threshold briefly if at all. The mean electron energies also dip below the threshold for the faster pulses. Only the 80-kA/ns pulse maintains energies favorable for ionization, resulting in an order of magnitude more ions even as $H_2$ is still desorbing.

The differences in the electron and $H^+$ energies result from the reverse polarity of the coaxial line for which the cathode heats and desorbs before the anode. The electrons are accelerated toward the anode while the ions are drawn into the gap by the electrons. This results in a non-neutral charge distribution in the gap which, with the **E**-field exclusion of the plasma layer, creates the field profiles in Fig. 7(a).

The first conclusion is that the plasma formation rate is the confluence of the **B** field and desorption rate (Fig. 4), the ionization rates (Fig. 2), and the **E** field. The **B** field heats the electrode surfaces while restraining $v_{\text{drift}}$. The applied **E** radially accelerates the particles from the surface of the plasma. Because the **B** field rapidly diffuses through a $10^{17}$-cm$^{-3}$ plasma ($1/\mu\sigma_\perp \sim 10^5$–$10^8$ m$^2$/s depending on $T_e$ and **B**), particles are not Ohmically heated.

The second conclusion is that for a given segment of transmission line operated at increased current densities, there is no catastrophic power-flow failure mechanism that is activated once a pulse-rise or current-density threshold is breached. The contaminant inventory is fixed while the ionization rate is reduced with increasing pulse rise. There is also increased magnetic confinement at higher current, discussed in Sec. IV. However, the total current loss in the system will increase as currents are increased due to the accumulation of plasma in the AK gap that has desorbed from surfaces upstream. The net inventory of plasma is a function of the total heated surface area and this increases with peak current.

### C. Assumption of desorbed plasma

The simulations of the Z Accelerator reported in Refs. [31,32], and [18] use a reduced model of plasma formation in which the desorbed neutrals are fully ionized

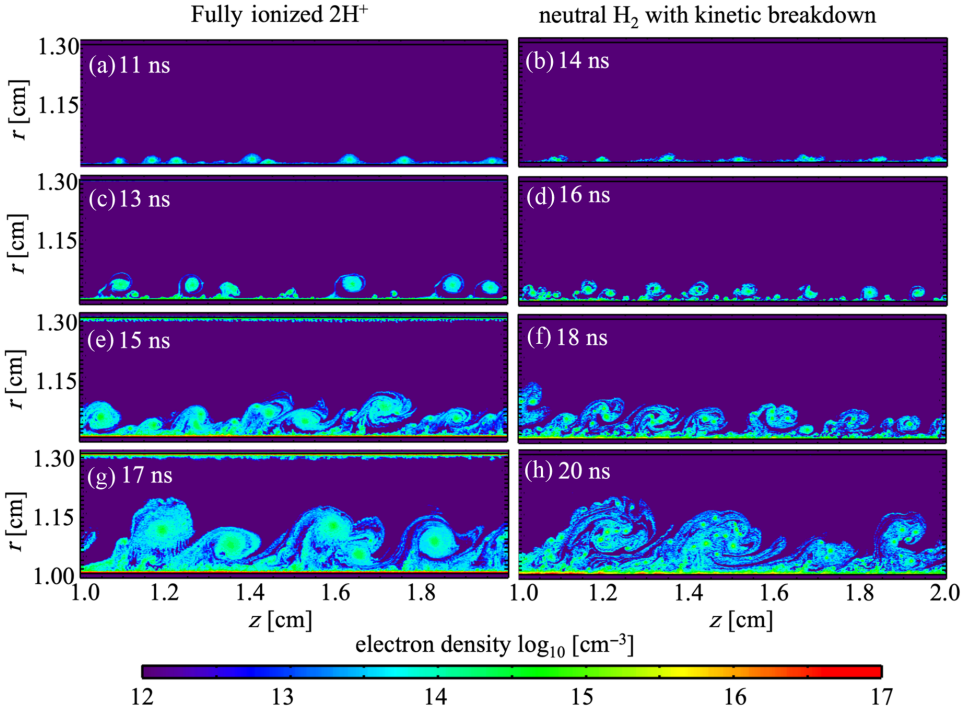


FIG. 9. The electron density contours that result when full ionization is assumed (left) and when the ionization of desorbed contaminants is modeled (right). The fully ionized and kinetic-breakdown models are shown 4 times early in the 280-kA/ns pulse rise to demonstrate evolution. The density distributions from the breakdown model at (b) 14, (d) 16, (f) 18, and (h) 20 ns are comparable in radial extent to the fully ionized contours taken 3 ns earlier in the pulse (a) 11, (c) 13, (e) 15, and (g) 17 ns, respectively).

within three grid cells from the surface. A direct comparison is made here between the fully ionized assumption and kinetic breakdown using the Z-relevant 280 kA/ns pulse rise. Figure 9 compares the densities at four snapshots during the pulse for the two plasma formation techniques. When breakdown is modeled, the density distributions lag the fully ionized assumption by $\sim 3$ ns.

The similar densities in the AK gap are another indication that transport is driven by conditions in the lower-density outer sheath and not those near the electrode surface. The bulk of the plasma in the fully ionized model lies on the electrode surface, barely discernible in Fig. 9(g). This makes the transport process insensitive to the number of assumed monolayers.

## IV. PLASMA TRANSPORT

Over the range of current pulses considered (8, 28, and 48 MA in 100 ns), the collision rates from Eq. (3) are 3 to 7 orders of magnitude below $\omega_{ce}$. In this regime, transport is inhibited perpendicular to the magnetic field and the contributions from the off-diagonal elements of the transport coefficients [86] become significant [87]. Using the fluid approximation of the generalized Ohm's law [88,89]:

$$\mathbf{j} = \sigma \mathbf{E}'_{\parallel} + \sigma_{\perp} \mathbf{E}'_{\perp} + \sigma_H (\mathbf{b} \times \mathbf{E}'_{\perp}),$$

where $\mathbf{E}'$ is the effective electric field in the ion inertial frame, the tensor elements are

$$\sigma = \frac{ne^2}{m\nu_c}$$
$$\sigma_{\perp} = \frac{\sigma}{1 + \frac{\omega_c^2}{\nu_c^2}} \quad \text{and,}$$
$$\sigma_{\wedge} = \sigma_H = \sigma_{\perp} \frac{\omega_c}{\nu_c}. \tag{6}$$

$\sigma_H$ is the off-diagonal Hall conductivity that establishes a current perpendicular to $\mathbf{E}'$ and $\mathbf{B}$.

This fluid approximation was previously applied to multi-MA transport [18], concluding that current loss is well approximated as a Hall current and that the off-diagonal plasma diffusion rate has the same dependence on $\omega_c/\nu_c$ as Eq. (6):

$$D_H = \frac{k_B T}{m\nu_c \left(1 + \frac{\omega_c^2}{\nu_c^2}\right)} = \frac{\omega_c}{\nu_c} \simeq \frac{k_B T}{eB},$$

which is Bohm-like diffusion [90]. The diffusion of the plasmas in Fig. 5 also appears inversely proportional to $B$. Unfortunately, a more definitive statement is not possible because estimates of the diffusion rates are complicated by

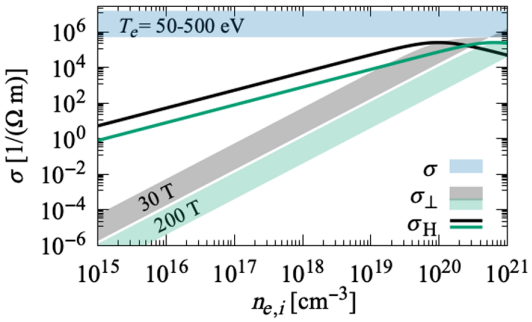


FIG. 10. The electrical conductivity tensor elements for $\bar{Z} = 1$ [Eq. (6)] as functions of plasma density in the electron temperature range 50–500 eV and with $B_\theta = 30$ (black) or 200 T (green).

the other physics modeled, such as ionization, the applied **E**, instabilities, and charge exchange.

As a plasma becomes collisional, the transport coefficients converge to their scalar values. This is illustrated in Fig. 10 for $\bar{Z} = 1$. The conductivities in Eq. (6) are plotted as functions of plasma density using $T_e = 50$–500 eV and $B_\theta = 30$ and 200 T [motivated by Figs. 7(b) and 8]. The two values of $B_\theta$ demonstrate how cross-gap currents are reduced with increasing $B$. Conversely, the magnetic field diffusion rate, $1/\mu\sigma_\perp$, increases with increasing $B$, explaining the absence of conducting plasmas in Fig. 7(b).

## V. MELT TRANSITION

While the peak plasma densities are constrained by the effective contaminant inventory during the breakdown, the available plasma inventory increases by $10^4$ as the inner-radius electrodes eventually melt and ionize. Melt occurs out to $r \simeq 4$ cm at 20 MA from Joule heating alone. The dynamics of electrode melt as a function of radius is investigated without kinetic effects using the ALEGRA arbitrary Lagrangian-Eulerian MHD code [91].

The simulation geometry is a 2D $(r, z)$ radially converging transmission line with a 3-mm AK gap, representative of the feed portion of the MITL in Fig. 1(a) without the coaxial segment. The full $Z$-pinch pulse is modeled, using a realistic pulse from the $Z$ accelerator. The simulation geometry and the current pulse are shown in Fig. 11(a). The electrodes are modeled using a stainless steel (SS) equation-of-state with 10-μm resolution. The density floor is 0.1 kg/m$^3$ ($\sim 10^{18}$ cm$^{-3}$) and the MHD solution includes conduction and radiation transport.

The evolution of the electrode density is represented in Fig. 11. Density contour maps are shown 4 times during the pulse beginning at 5 MA, when melt reaches $r \simeq 1$ cm. [SS melts near 1700 K, or 104 T from Eq. (1) assuming a linear pulse rise].

Figure 11(a) demonstrates that long after melt, there is insignificant transport of the near-solid-density plasma into the AK gap. The density profile of the electrode is shown in

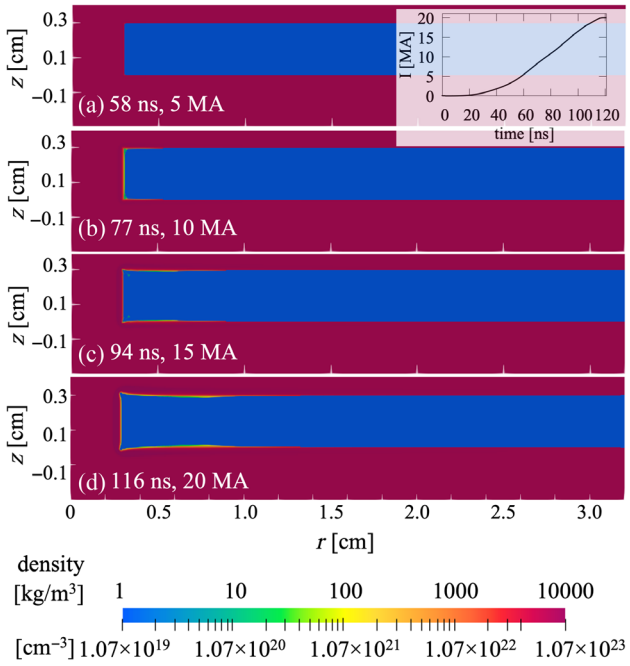


FIG. 11. The electrode density contours from MHD at 4 times during the pulse, which shown for reference in the top right inset. The times and corresponding currents are noted for (a) 58 ns/5 MA, (b) 77 ns/10 MA, (c) 94 ns/15 MA, and (d) 116 ns/20 MA.

more detail in Fig. 12(a), with line-outs at $r = 1$ cm. The dense bulk-electrode plasma sits in a different transport regime than the tenuous surface plasmas generated prior to melt. The bulk-electrode plasmas conduct and, subject to $\mathbf{j} \times \mathbf{B}$, experience more compression than expansion into the AK gap. Expansion eventually occurs at $r = 1$ cm, near peak current and in the 100-μm range.

The diffusion of the magnetic field into the electrode bulk is plotted in Fig. 12(b). This diffusivity contrasts with

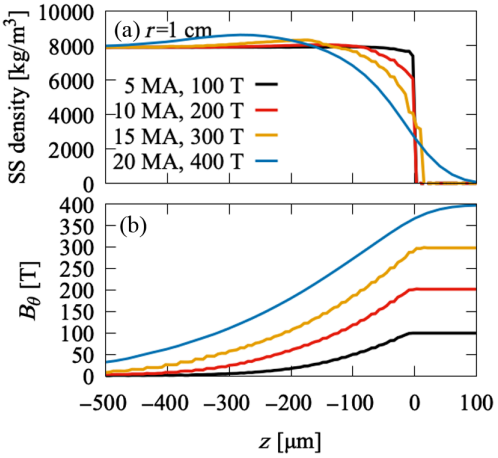


FIG. 12. The electrode (a) density and (b) magnetic field at $r = 1$ cm for the radial transmission line in Fig. 11. The values are plotted at 4 times during the pulse corresponding to $B_\theta = 100$, 200, 300, and 400 T.

the $< 10^{17}$ cm$^{-3}$-density reliance on off-diagonal elements in Fig. 10. Simulations at 50 MA indicate that the electrode melt and motion scale with local $B^2$; the affected surface area increases but there is still no significant plasma diffusion into the gap in a 2D model. This MHD treatment does not consider the diffusion of hydrogen from the bulk, which will be discussed in future work.

## VI. CONCLUSION

The detailed generation and evolution of electrode plasmas were examined here using fully relativistic, Monte Carlo particle-in-cell (PIC) and magnetohydrodynamic (MHD) simulations over a range of peak currents. The PIC calculations, informed by vacuum science, describe the electrode surface breakdown and particle transport prior to electrode melt. The MHD calculations show the bulk electrodes impacted by melt.

Past results from vacuum science indicate that the primary electrode contaminants are water and hydrogen. As electrode temperatures rise, outgassing becomes dominated by hydrogen adsorbed on and absorbed into the electrode metal lattice. For a pulsed-power system with increasing surface temperatures, this provides a contaminant inventory that exceeds the maximum surface coverage defined by a monolayer but is limited by an expected bulk concentration of $\sim 10^{19}$ cm$^{-3}$.

This inventory was used to initialize kinetic simulations of surface breakdown. Monte Carlo PIC simulations were conducted from first principles, including 13 inelastic interactions, for peak currents of 8, 28, and 48 MA in 100 ns. While electrode contaminants desorb earlier and more rapidly at higher peak currents, the Arrhenius equation functions somewhat as a switch that rapidly asymptotes to a peak desorption rate. The electrodes are depleted of contaminants for all three pulses for our choice of 16 ML.

The desorbed neutrals rapidly ionize, forming a $10^{15}$–$10^{18}$ cm$^{-3}$ plasma that is effectively resistive while weakly collisional because it is created within, and rapidly penetrated by, a strong magnetic field ($> 30$ T). This plasma is not carrying significant current and does not Ohmically heat. Particle kinetic energy is instead increased by the applied electric field, which is able to penetrate the outer sheath of the plasma. The plasma adjacent to the electrode surface may reach $10^{19}$ cm$^{-3}$, but only the lower-density plasma at the extent of the sheath is accelerated into the AK gap. The $q\mathbf{E}$ force and charge exchange aid plasma transport into the AK gap. The magnetic field inhibits it. This surface plasma must be treated kinetically.

The plasma conditions generated by surface breakdown and by melt are differentiated by density and temperature. The melting electrodes form a conducting plasma ($10^{21}$–$10^{23}$ cm$^{-3}$) that experiences $\mathbf{j} \times \mathbf{B}$ compression and a typical decaying magnetic diffusion profile. The skin-depth ($l_s$) penetration of the electric field is sub-μm for plasma densities $\gtrsim 3 \times 10^{21}$ cm$^{-3}$, confirming that the physics of the bulk metal is well captured by MHD.

Exceptions to this physical description may arise from conductor ablation that generates plasmas in the $10^{19}$–$10^{21}$ cm$^{-3}$ range. Sources of ablation include material defects, the electrothermal instability, and wire-array-like electrode configurations. The *Z*-pinch loads that terminate the transmission lines are also not described here. The physics at the load is dominated by rapid melt from magnetic fields in excess of 300 T and is typically captured in MHD models of the pinch.

Increasing the current pulse magnitude by over a factor of 6 did not increase the density of the plasma transported from the electrode surface into the AK gap. Although neutral contaminants desorb more rapidly at increased current density, ionization is slower and the transport must occur perpendicular to a larger magnetic field. The resulting plasma densities in the AK gap are not significantly sensitive to the peak current for identical rise times.

The transmission lines modeled here are relevant to the low-inductance lines driving short-circuit, *Z*-pinch loads. For these systems, there is no inherent early-time catastrophic failure arising from electrode plasmas as the current density in the system is increased. In higher-power *Z*-pinch drivers, plasmas will form out to larger radii and will contribute to the current loss. This is a design issue but not a fundamental limitation.

Models of hydrogen diffusion through the bulk metal, ablation, electrode desorption, and vaporization are in progress. These processes may impact the current delivered to the load and the physics of the load implosion.

## ACKNOWLEDGMENTS

Special thanks are extended to Ron Goeke for technical advice on material outgassing and to George Laity and Mark Hess for the power-flow experimental platform. Sandia National Laboratories is a multi-mission laboratory managed and operated by National Technology & Engineering Solutions of Sandia, LLC., a wholly owned subsidiary of Honeywell International, Inc., for the U.S. Department of Energy's National Nuclear Security Administration under Contract No. DE-NA0003525. The views expressed in the article do not necessarily represent the views of the U.S. Department of Energy or the U.S. Government. This project was supported by LDRD project 226078.

[1] R. B. Spielman *et al.*, Phys. Plasmas **5**, 2105 (1998).
[2] V. V. Aleksandrov, E. V. Grabovski, A. N. Gribov, G. M. Oleinik, A. A. Samokhin, and P. V. Sasorov, Plasma Phys. Rep. **34**, 911 (2008).
[3] W. A. Stygar *et al.*, Phys. Rev. ST Accel. Beams **12**, 120401 (2009).

[4] W. Zou, F. Guo, L. Chen, S. Song, M. Wang, W. Xie, and J. Deng, Phys. Rev. ST Accel. Beams **17**, 110401 (2014).
[5] J. Deng *et al.*, Matter Radiat. Extremes **1**, 48 (2016).
[6] S. A. Sorokin, Phys. Plasmas **23**, 043110 (2016).
[7] R. W. Lemke, D. H. Dolan, D. G. Dalton, J. L. Brown, K. Tomlinson, G. R. Robertson, M. D. Knudson, E. Harding, A. E. Mattsson, J. H. Carpenter, R. R. Drake, K. Cochrane, B. E. Blue, A. C. Robinson, and T. R. Mattsson, J. Appl. Phys. **119**, 015904 (2016).
[8] I. Langmuir, Phys. Rev. **2**, 450 (1913).
[9] R. Fowler and L. Nordheim, Proc. R. Soc. A **119**, 173 (1928).
[10] M. R. Gomez, R. M. Gilgenbach, M. E. Cuneo, C. A. Jennings, R. D. McBride, E. M. Waisman, B. T. Hutsel, W. A. Stygar, D. V. Rose, and Y. Maron, Phys. Rev. Accel. Beams **20**, 010401 (2017).
[11] A. Porwitzky, D. H. Dolan, M. R. Martin, G. Laity, R. W. Lemke, and T. R. Mattsson, Phys. Plasmas **25**, 063110 (2018).
[12] M. E. Savage, K. R. LeChien, M. R. Lopez, B. S. Stoltzfus, W. A. Stygar, D. S. Artery, J. A. Lott, and P. A. Corcoran, in *Proceedings of the 2011 IEEE Pulsed Power Conference, Chicago, IL* (IEEE, New York, 2011), pp. 983–990.
[13] D. B. Sinars *et al.*, Phys. Plasmas **27**, 070501 (2020).
[14] D. Jianjun, X. Weiping, F. Suping, W. Meng, L. Hongtao, S. Shengyi, X. Minghe, H. An, T. Qing, G. Yuanchao, G. Yongchao, W. Bin, Z. Wenkang, H. Xianbin, W. Lijuan, Z. Zhaohui, H. Yi, and Y. Libing, IEEE Trans. Plasma Sci. **41**, 2580 (2013).
[15] S. A. Chaikovsky, A. Chuvatin, and V. Oreshkin, Instrum. Exp. Tech. **55**, 209 (2012).
[16] A. A. Kim, B. M. Kovalchuk, V. A. Kokshenev, A. V. Shishlov, N. A. Ratakhin, V. I. Oreshkin, V. V. Rostov, V. I. Koshelev, and V. Losev, Matter Radiat. Extremes **1**, 201 (2016).
[17] D. H. Dolan, K. Bell, B. Fox, S. C. Jones, P. Knapp, M. R. Gomez, M. Martin, A. Porwitzky, and G. Laity, J. Appl. Phys. **123**, 034502 (2018).
[18] N. Bennett, D. R. Welch, G. Laity, D. V. Rose, and M. E. Cuneo, Phys. Rev. Accel. Beams **24**, 060401 (2021).
[19] J. M. Creedon, J. Appl. Phys. **46**, 2946 (1975).
[20] J. M. Creedon, J. Appl. Phys. **48**, 1070 (1977).
[21] C. W. Mendel, J. Appl. Phys. **50**, 3830 (1979).
[22] R. I. Lawconnell and J. Neri, Phys. Fluids B **2**, 629 (1990).
[23] N. Bruner, T. Genoni, E. Madrid, D. Rose, D. Welch, K. Hahn, J. Leckbee, S. Portillo, B. Oliver, V. Bailey, and D. Johnson, Phys. Rev. ST Accel. Beams **11**, 040401 (2008).
[24] N. Bruner, T. Genoni, E. Madrid, D. Welch, K. Hahn, and B. Oliver, Phys. Rev. ST Accel. Beams **12**, 070401 (2009).
[25] A. S. Richardson, J. C. Zier, J. T. Engelbrecht, S. B. Swanekamp, J. W. Schumer, D. Mosher, P. F. Ottinger, D. L. Duke, T. J. Haines, M. P. McCumber, and A. Gehring, Phys. Rev. Accel. Beams **22**, 050401 (2019).
[26] R. Elsey, Vacuum **25**, 299 (1975).
[27] M. Li and H. F. Dylla, J. Vac. Sci. Technol. A **11**, 1702 (1993).
[28] H. F. Dylla, Vacuum **47**, 647 (1996).
[29] M. Cuneo, IEEE Trans. Dielectr. Electr. Insul. **6**, 469 (1999).
[30] D. R. Welch, N. Bennett, T. C. Genoni, D. V. Rose, C. Thoma, C. Miller, and W. A. Stygar, Phys. Rev. Accel. Beams **22**, 070401 (2019).
[31] N. Bennett, D. R. Welch, C. A. Jennings, E. Yu, M. H. Hess, B. T. Hutsel, G. Laity, J. K. Moore, D. V. Rose, K. Peterson, and M. E. Cuneo, Phys. Rev. Accel. Beams **22**, 120401 (2019).
[32] D. R. Welch, N. Bennett, T. C. Genoni, C. Thoma, and D. V. Rose, Phys. Rev. Accel. Beams **23**, 110401 (2020).
[33] K. Leung, L. J. Criscenti, and A. C. Robinson, J. Phys. Condens. Matter **32**, 335101 (2020).
[34] E. P. Yu, M. E. Cuneo, M. P. Desjarlais, R. W. Lemke, D. B. Sinars, T. A. Haill, E. M. Waisman, G. R. Bennett, C. A. Jennings, T. A. Mehlhorn, T. A. Brunner, H. L. Hanshaw, J. L. Porter, W. A. Stygar, and L. I. Rudakov, Phys. Plasmas **15**, 056301 (2008).
[35] T. J. Awe, E. P. Yu, M. W. Hatch, T. M. Hutchinson, K. Tomlinson, W. D. Tatum, K. C. Yates, B. T. Hutsel, and B. S. Bauer, Phys. Plasmas **28**, 072104 (2021).
[36] M. Johnston, S. Patel, G. Laity, M. Cuneo, R. Doron, E. Stambulchik, V. Bernshtam, and Y. Maron, in *Proceedings of the 63rd Annual Meeting of the APS Division of Plasma Physics* (2019), Vol. 2019, YP10.060, https://ui.adsabs.harvard.edu/abs/2019APS..DPPY10060J.
[37] D. Zimmer, F. Conti, F. Beg, M. Gomez, C. Jennings, C. Myers, and N. Bennett, Phys. Plasmas (to be published).
[38] C. Myers, C. Jennings, and N. Bennett, Phys. Plasmas (to be published).
[39] R. Elsey, Vacuum **25**, 347 (1975).
[40] M. Bernardini *et al.*, J. Vac. Sci. Technol. A **16**, 188 (1998).
[41] M. Jones, RGA measurement on Sandia National Laboratories' Z Machine (unpublished).
[42] C. Park, T. Ha, and B. Cho, J. Vac. Sci. Technol. A **34**, 021601 (2016).
[43] J. M. D. Lane, K. Leung, A. P. Thompson, and M. E. Cuneo, J. Phys. Condens. Matter **30**, 465002 (2018).
[44] H. Dylla, J. Nucl. Mater. **93–94**, 61 (1980).
[45] Y. Yagodzinskyy, O. Todoshchenko, S. Papula, and H. Hänninen, Steel Res. Int. **82**, 20 (2011).
[46] R. Calder and G. Lewin, Br. J. Appl. Phys. **18**, 1459 (1967).
[47] Y. Ishikawa and T. Yoshimura, J. Vac. Sci. Technol. A **13**, 1847 (1995).
[48] H. F. Dylla, D. M. Manos, and P. H. LaMarche, J. Vac. Sci. Technol. A **11**, 2623 (1993).
[49] K. Leung, R. Goeke, A. Ilgen, A. Wilson, and N. Bennett (to be published).
[50] C. Birdsall, IEEE Trans. Plasma Sci. **19**, 65 (1991).
[51] C. Thoma, T. P. Hughes, N. L. Bruner, T. C. Genoni, D. R. Welch, and R. E. Clark, IEEE Trans. Plasma Sci. **34**, 910 (2006).
[52] D. V. Rose, D. R. Welch, R. E. Clark, C. Thoma, W. R. Zimmerman, N. Bruner, P. K. Rambo, and B. W. Atherton, Phys. Plasmas **18**, 093501 (2011).
[53] D. Welch, D. Rose, B. Oliver, and R. Clark, Nucl. Instrum. Methods Phys. Res., Sect. A **464**, 134 (2001).
[54] D. R. Welch, D. V. Rose, R. E. Clark, T. C. Genoni, and T. P. Hughes, Comput. Phys. Commun. **164**, 183 (2004).

[55] D. Welch, T. Genoni, R. Clark, and D. Rose, J. Comput. Phys. **227**, 143 (2007).

[56] C. Thoma, D. R. Welch, R. E. Clark, D. V. Rose, and I. E. Golovkin, Phys. Plasmas **24**, 062707 (2017).

[57] T. C. Genoni, R. E. Clark, and D. R. Welch, Open Plasma Phys. J. **3**, 36 (2010).

[58] C. K. Birdsall and A. B. Langdon, *Plasma Physics via Computer Simulation* (Adam Hilger, New York, 1991).

[59] B. B. Godfrey, Time-biased field solver for electromagnetic codes, Technical Report No. AMRC-N-138, Naval Research Laboratory Washington, D. C., 1980.

[60] H. Knoepfel, *Magnetic Fields* (John Wiley and Sons, New York, 2000).

[61] J. Valencia and P. Quested, in *ASM Handbook Castings ASM International, Materials Park* (2008), https://materialsdata.nist.gov/bitstream/handle/11115/166/Thermophysical%20Properties.pdf?isAllowed=y&sequence=3.

[62] W. A. Stygar, S. E. Rosenthal, H. C. Ives, T. C. Wagoner, G. O. Allshouse, K. E. Androlewicz, G. L. Donovan, D. L. Fehl, M. H. Frese, T. L. Gilliland, M. F. Johnson, J. A. Mills, D. B. Reisman, P. G. Reynolds, C. S. Speas, R. B. Spielman, K. W. Struve, A. Toor, and E. M. Waisman, Phys. Rev. ST Accel. Beams **11**, 120401 (2008).

[63] J. G. Hust and A. B. Lankfor, *Standard Reference Materials* (Gaithersburg, MD, 1984), https://nvlpubs.nist.gov/nistpubs/Legacy/SP/nbsspecialpublication260-90.pdf.

[64] W. Leo, *Techniques for Nuclear and Particle Physics Experiments*, 2nd ed. (Springer-Verlag, Berlin, Heidelberg, 1994).

[65] D. V. Rose, E. A. Madrid, D. R. Welch, R. E. Clark, C. B. Mostrom, W. A. Stygar, and M. E. Cuneo, Phys. Rev. ST Accel. Beams **18**, 030402 (2015).

[66] T. W. L. Sanford, J. A. Halbleib, J. W. Poukey, A. L. Pregenzer, R. C. Pate, C. E. Heath, R. Mock, G. A. Mastin, D. C. Ghiglia, T. J. Roemer, P. W. Spence, and G. A. Proulx, J. Appl. Phys. **66**, 10 (1989).

[67] K. Nanbu and S. Yonemura, J. Comput. Phys. **145**, 639 (1998).

[68] P. W. Rambo and R. J. Procassini, Phys. Plasmas **2**, 3130 (1995).

[69] P. Redhead, *The Physical Basis for Ultrahigh Vacuum* (Chapman and Hall, London, 1968).

[70] M. E. Cuneo, P. R. Menge, D. Hanson, W. Fowler, M. Bernard, G. Ziska, A. Filuk, T. Pointon, R. Vesey, D. Welch, J. E. Bailey, M. Desjarlais, T. Lockner, T. Mehlhorn, S. Slutz, and M. Stark, IEEE Trans. Plasma Sci. **25**, 229 (1997).

[71] B. T. Hutsel, P. A. Corcoran, M. E. Cuneo, M. R. Gomez, M. H. Hess, D. D. Hinshelwood, C. A. Jennings, G. R. Laity, D. C. Lamppa, R. D. McBride, J. K. Moore, A. Myers, D. V. Rose, S. A. Slutz, W. A. Stygar, E. M. Waisman, D. R. Welch, and B. A. Whitney, Phys. Rev. Accel. Beams **21**, 030401 (2018).

[72] D. R. Welch, S. A. Cohen, T. C. Genoni, and A. H. Glasser, Phys. Rev. Lett. **105**, 015002 (2010).

[73] D. R. Welch, D. V. Rose, C. Thoma, R. E. Clark, C. Miller, E. A. Madrid, W. R. Zimmerman, P. K. Rambo, J. Schwarz, M. Savage, and B. W. Atherton, Phys. Plasmas **20**, 083108 (2013).

[74] N. Bennett, M. Blasco, K. Breeding, V. DiPuccio, B. Gall, M. Garcia, S. Gardner, J. Gatling, E. C. Hagen, A. Luttman, B. T. Meehan, S. Molnar, R. O'Brien, E. Ormond, L. Robbins, M. Savage, N. Sipe, and D. R. Welch, Phys. Plasmas **24**, 062705 (2017).

[75] Y.-K. Kim and M. E. Rudd, Phys. Rev. A **50**, 3954 (1994).

[76] G. H. Dunn and B. Van Zyl, Phys. Rev. **154**, 40 (1967).

[77] M. B. Shah and H. B. Gilbody, J. Phys. B **14**, 2361 (1981).

[78] W. Ott, E. Speth, and the W7-AS Team, Nucl. Fusion **42**, 796 (2002).

[79] C. McGrath, M. B. Shah, P. C. E. McCartney, and J. W. McConkey, Phys. Rev. A **64**, 062712 (2001).

[80] W. L. Fite, R. T. Brackmann, and W. R. Snow, Phys. Rev. **112**, 1161 (1958).

[81] C. Bottcher, J. Phys. B **9**, 2899 (1976).

[82] Y.-K. Kim and J.-P. Desclaux, Phys. Rev. A **66**, 012708 (2002).

[83] J.-S. Yoon, M.-Y. Song, J.-M. Han, S. H. Hwang, W.-S. Chang, B. Lee, and Y. Itikawa, J. Phys. Chem. Ref. Data **37**, 913 (2008).

[84] H. Tawara, Y. Itikawa, H. Nishimura, and M. Yoshino, J. Phys. Chem. Ref. Data **19**, 617 (1990).

[85] C. J. Latimer, K. F. Dunn, F. P. O'Neill, M. A. MacDonald, and N. Kouchi, J. Chem. Phys. **102**, 722 (1995).

[86] R. Balescu, *Transport Processes in Plasmas* (North Holland, Amsterdam, 1988).

[87] M. R. Weis, A. J. Harvey-Thompson, and D. E. Ruiz, Phys. Plasmas **28**, 012705 (2021).

[88] S. I. Braginskii, in *Reviews of Plasma Physics*, Vol. 1, edited by M. A. Leontovich (Consultants Bureau, New York, 1965), p. 205.

[89] B. V. Somov, *Plasma Astrophysics: Part I Fundamentals and Practice* (Springer Science+Business Media, LLC, New York, 2006).

[90] D. Bohm, in *The Characteristics of Electrical Discharges in Magnetic Fields*, edited by A. Guthrie and R. Wakerling (McGraw-Hill, New York, 1949), Chap. 2.

[91] A. Robinson *et al.*, in *Proceedings of the 46th AIAA Aerospaces Sciences Meeting* (2008), 10.2514/6.2008-1235.